Analysis of the charging kinetics in silver nanoparticles-silica nanocomposite dielectrics at different temperatures

C Djaou, C Villeneuve-Faure, Kremena Makasheva, Laurent Boudou, G Teyssedre

IOP Publishing Nano Express 2 (2021) 044001 https://doi.org/10.1088/2632-959X/ac3886

NANO EXPRESS

PAPER

Analysis of the charging kinetics in silver nanoparticles-silica nanocomposite dielectrics at different temperatures

C Djaou, C Villeneuve-Faure*, K Makasheva*, L Boudou and G Teyssedre

LAPLACE, Université de Toulouse, CNRS, INPT, UPS, Toulouse, France

* Author to whom any correspondence should be addressed.

E-mail: christina.villeneuve@laplace.univ-tlse.fr **and** kremena.makasheva@laplace.univ-tlse.fr

Keywords: charge trapping, nanodielectric, thin films, plasma processes, KPFM

OPEN ACCESS

RECEIVED
21 September 2021

REVISED
8 November 2021

ACCEPTED FOR PUBLICATION
9 November 2021

PUBLISHED
22 November 2021

Abstract

Dielectric nanocomposite materials are now involved in a large panel of electrical engineering applications ranging from micro-/nano-electronics to power devices. The performances of all these systems are critically dependent on the evolution of the electrical properties of the dielectric parts, especially under temperature increase. In this study we investigate the impact of a single plane of silver nanoparticles (AgNPs), embedded near the surface of a thin silica (SiO_2) layer, on the electric field distribution, the charge injection and the charge dynamic processes for different AgNPs-based nanocomposites and various temperatures in the range 25°C–110°C. The electrical charges are injected locally by using an Atomic Force Microscopy (AFM) tip and the related surface potential profile is probed by Kelvin Probe Force Microscopy (KPFM). To get deeper in the understanding of the physical phenomena, the electric field distribution in the AgNPs-based nanocomposites is computed by using a Finite Element Modeling (FEM). The results show a strong electrostatic coupling between the AFM tip and the AgNPs, as well as between the AgNPs when the AgNPs-plane is embedded in the vicinity of the SiO_2-layer surface. At low temperature (25°C) the presence of an AgNPs-plane close to the surface, i.e., at a distance of 7 nm, limits the amount of injected charges. Besides, the AgNPs retain the injected charges and prevent from charge lateral spreading after injection. When the temperature is relatively high (110°C) the amount of injected charges is increased in the nanocomposites compared to low temperatures. Moreover, the speed of lateral charge spreading is increased for the AgNPs-based nanocomposites. All these findings imply that the lateral charge transport in the nanocomposite structures is favored by the closely situated AgNPs because of the strong electrostatic coupling between them, additionally activated by the temperature increase.

1. Introduction

Any of the future directions of development of micro-/nano-electronics, beyond-Complementary Metal Oxide Semiconductor (CMOS) systems or sensors, requires scaling down the size of developed devices, reducing their energy consumption and refining their performances under enlarged environmental constraints (temperature variations, humidity, exposure to intense light, etc.) As clearly indicated in a recent roadmap for European Nanoelectronics a major challenge would be to solve issues related to energy losses and heating, with the latter potentially leading to a strong evolution of the electrical characteristics of the device [1]. To overcome these problems rational engineering and characterization of new materials, like core–shell nanomaterials [2, 3], 2D-materials (for example MoS_2) [4], alternative channel materials for CMOS, high-k dielectrics [5, 6], multi-gates, thin layers, heterostructures, etc., are timely due. Dielectric nanocomposite materials appear as promising way to improve devices properties in various applications, from micro-/nano-electronics [7, 8] to microsystems [9] or power engineering devices [10]. For example, Si nanocrystals embedded in a silica matrix could replace the floating gate in nonvolatile flash memory devices, thus reducing the leakage current and increasing reliability of the device, as the spatial localization of the stored charges is improved [11–13]. Moreover, metal-containing

nanocomposites (NCs) based on dielectric matrices with embedded metal nanoparticles (NPs) have demonstrated unique magnetic [14], plasmonic [15, 16] and dielectric [1, 17–22] properties, compared to the matrix alone. These properties are strongly related to the amount of inserted metal NPs, and consequently to the film morphology. Tuning of the electrical properties in a very broad range can be achieved by controlling the size, density, and distribution of metal nanoparticles:

(i) NCs with low metal volume fractions (around 5%) and randomly dispersed metal-NPs in the dielectric matrix [17–23] express a dielectric-like behavior under applied electric field [1, 19–22]. The charge injection and trapping dynamics are controlled by both the ability of metal-NPs to store electrical charges as artificial deep trapping centers and the properties of the surrounding dielectric matrix, in terms of density of charge trapping centers and their energy level distribution, in the frame of the space charge limited conduction mechanism (SCLC) [15–22].

(ii) NCs with an amount of the metal-NPs ranging from medium to high concentrations (10%–25% of metal volume fractions) [19–21] keep the dielectric-like behaviour with a space charge limited conduction. However, at high electric field they present a steep variation of the current-voltage characteristics. The observed very strong current increase in a relatively narrow voltage range appears because the charge injection and transport in these NCs are favored by electron tunneling between the nanoparticles, in the presence of a strongly increased number of free electrons provided by the trap-filled limit in the dielectric matrix.

(iii) a percolated network of metal-NPs in the dielectric matrix. In metal-containing NCs the electrical percolation threshold is found to appear at metal volume fractions around 30% [19–21, 23, 24]. Due to the metal percolated chain formed by physically connected NPs a metallic regime of conduction is observed for these NCs.

The above mentioned and other functionalities of metal-containing NCs can be obtained when properly designing the material. Depending on the structural parameters of the NCs the electrical transport character can be changed from an energy activated type with a negative temperature coefficient of resistivity (TCR) to a metallic one with positive TCR, with a smooth transition between the two types [20, 24]. Indeed, the DC resistivity of silver-silica NCs, prepared by electrodeposition method, was found to exhibit a transition from metallic regime in the very low temperature range (100–180 K) to a semiconductor-like when increasing the temperature in the temperature range region (180–300 K) [24]. In general, the temperature constraints appear challenging in sustaining the electrical behaviour of dielectric materials for a large number of nanoelectronic devices [1, 25]. For example, the dielectric capacitor applications require stable performance at working temperatures of around 80°C for power factor maintaining, around 140°C for Hybrid Electric Vehicle (HEV), or in the range of −50°C–250°C for aerospace applications [25]. Given that thermally activated diffusion of metal atoms and/or very small metal NPs can occur in the high temperature range the NCs containing metal NPs require probing of their electrical behaviour as a function of the temperature. According to the reported in the literature data for the activation energy of silver (1.24 eV in the 275°C–365°C range) the Ag diffusion length in amorphous silica would increase from a few nanometers to a few hundredths of nanometers for 1h at 300°C [26–28]. On the other side, considering this activation energy, the Ag diffusion length in silica at temperatures below 150°C would be limited to less than a nanometer for the same time scale. In this work our choice was to stay within the medium temperature range (less than 150°C), aiming at to avoid metal diffusion effects when analyzing the charging kinetics in AgNPs-silica NCs dielectrics at different temperatures.

To qualify the electrical performance and reliability of NCs under different types of stress, their characterization should involve studies of the processes occurring at the interfaces between different phases in the material, and more generally at the nanoscale. In the last decade, investigation at nanoscale of the electrical properties of NCs has been achieved by applying electrical modes derived from Atomic Force Microscopy (AFM), since they appear well-adapted and extremely powerful. Indeed, Electrostatic Force Microscopy (EFM), Kelvin Probe Force Microscopy (KPFM) or Conductive AFM (C-AFM) were extensively used to characterize the dielectric behaviour of thin films at nanoscale level providing relevant information on the dielectric permittivity [29, 30], charge injection, trapping [31, 32] and transport [33]. By using these tools, the influence of metal-NPs on the charge trapping dynamic has been revealed. For example, Lwin *et al* demonstrated, via KPFM measurements, that after local charge injection, Pt-NPs embedded in SiO_2 matrix improve positive charge trapping time, when compared to Au-NPs [31]. Moreover, Schaadt *et al*, showed through EFM that the positive carriers exhibit longer trapping time compared to the negative ones for Co-NPs embedded in SiO_2 matrix [32]. However, temperature dependent behavior of the NCs at nanoscale is rarely considered in the reported in the literature studies. To bring information on the subject and fill the gap the present paper reports on the impact of

temperature and/or the nanoparticles position in the dielectric matrix on the charge injection and kinetics. In this work, silica-based AgNPs containing NCs are investigated. A single plane of AgNPs is embedded in a SiO_2 matrix at a controlled distance from the surface. This stratified structure presents the advantage of simplifying issues related to the AgNPs location in the volume and to eventual interactions between the AgNPs dispersed in the volume. Thus, it reduces the 3-dimentional (3D-) problem to a 2D-one and provides information on the influence of the AgNPs on the electric field distribution. The charge injection and kinetic analyses are performed at nanoscale by using KPFM mode.

2. Materials and methods

2.1. Plasma process and operating conditions for deposition of the AgNPs-based NCs

In this work we have investigated NCs that contain a plane of AgNPs. The AgNPs were embedded in a thin silica (SiO_2) layer at a depth which is called hereafter d_c. The NC structure thickness is noted d_{tot} (figure 1). All parameters characterizing the elaborated NCs are well controlled via the parameters of the plasma deposition process. The synthesis of the NCs was performed in a capacitively-coupled plasma, generated in the RF range (13.56 MHz). The plasma process was maintained at low pressure [17, 34]. A strong particularity of the applied plasma process is its axially-asymmetric design. The RF-driven electrode is smaller in size (10 cm in diameter). It is made of silver to bear the sputtering process. The grounded electrode is larger (12 cm in diameter), made of stainless steel. The distance between the two electrodes is 3.5 cm. The reactor walls, made of stainless steel, were grounded too. Due to the geometrical asymmetry between the powered electrode (small electrode) and the grounded parts of the reactor (large electrode and reactor walls), the produced plasma induces a self-bias voltage (V_{dc}) on the RF-driven electrode (the silver electrode). This self-bias voltage is at the origin of the silver sputtering. Since in the current reactor configuration the self-bias voltage is negative it accelerates the positive ions in the plasma toward the silver electrode, performing thus the silver sputtering. The self-bias voltage is proportional to the injected in the plasma power, so at a given pressure, the amount of silver, and thus the size of the AgNPs, is controlled by the applied plasma power.

To create the NCs containing AgNPs-plane we have used Si-substrates covered by 150–180 nm-thick thermal SiO_2-layers. The NC stratified structure was obtained after silver sputtering to synthesize the AgNPs and plasma polymerization to cover the AgNPs, thus embedding them in the silica matrix at the requested depth. The silver sputtering was performed for a time of 5 s in an argon plasma maintained at a pressure of $p = 5.4$ Pa with a RF power of $P = 80$ W. The self-bias voltage in this case was $V_{dc} = -1000$ V. The silica matrix that embed the AgNPs was obtained in the same plasma reactor in the plasma maintained by injected power of $P = 120$ W in argon, with admixture of hexamethyldisiloxane (HMDSO, $Si_2O(CH_3)_6$) and oxygen (O_2). The HMDSO precursor was injected by pulses, which makes the applied plasma process extremely versatile, with a fine tuning of the plasma parameters allowing elaboration of high quality silica matrices. The total gas pressure in the plasma reactor for silica deposition was $p_{tot} = 7.7$ Pa. The depth, at which the AgNPs were embedded in the SiO_2 matrix, was controlled through the silica deposition time. The silica sample alone was plasma deposited on a Si-substrate. One shall note here the very good reproducibility of the elaborated samples. More details on the reactor, the plasma process, the deposition procedure, and the plasma input parameters are given elsewhere [17, 34].

2.2. Structural characterization of the NCs

The NCs containing a single plane of AgNPs were visualized by Transmission Electron Microscopy (TEM) in cross-sectional and plane view images. Specimens transparent to electrons have been prepared according to a standard procedure: mechanical polishing and Ar^+ ion milling. The NCs and AgNPs parameters were extracted after image processing. The thickness of the SiO_2 matrix alone was measured by spectroscopic ellipsometry with a SE-2000 ellipsometer in the 250–850 nm spectral range with an incident angle of 75°. Forouhi-Bloomer dispersion law was applied to extract the thickness and the optical properties of the silica layers.

2.3. Electrical characterization of the NCs

AFM measurements were performed using a Bruker Multimode 8 apparatus. A silicon AFM tip with PtIr coating (curvature radius $R_c = 25$ nm and spring constant $k_s = 2.4$ Nm^{-1}) was used for the charge injection protocol and for the surface potential measurements by KPFM. After 10 min of dehydration at 110°C, the nanocomposite sample was placed in an environmentally controlled chamber (under N_2 atmosphere) to avoid charge dissipation due to the presence of a water layer on the sample surface. The dielectric charging was achieved in contact mode (contact force set to 30 nN) by applying positive or negative DC bias V_0 from −40 to +40 V (step of 10 V) to the AFM tip during 1 min. After the charging step, the same tip was used to probe the surface potential in Amplitude Modulation KPFM (AM-KPFM) mode using a 50 nm lift. During charge injection and

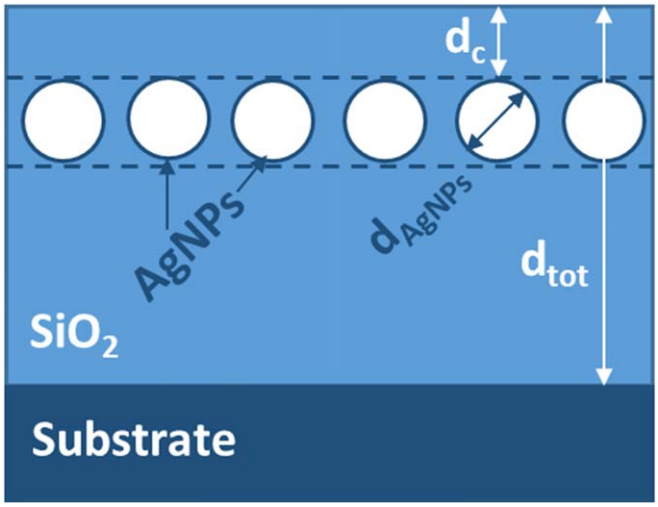

Figure 1. Scheme of the stratified structure of the nanocomposite: a plane of AgNPs inserted in thin SiO_2 layer at a given depth.

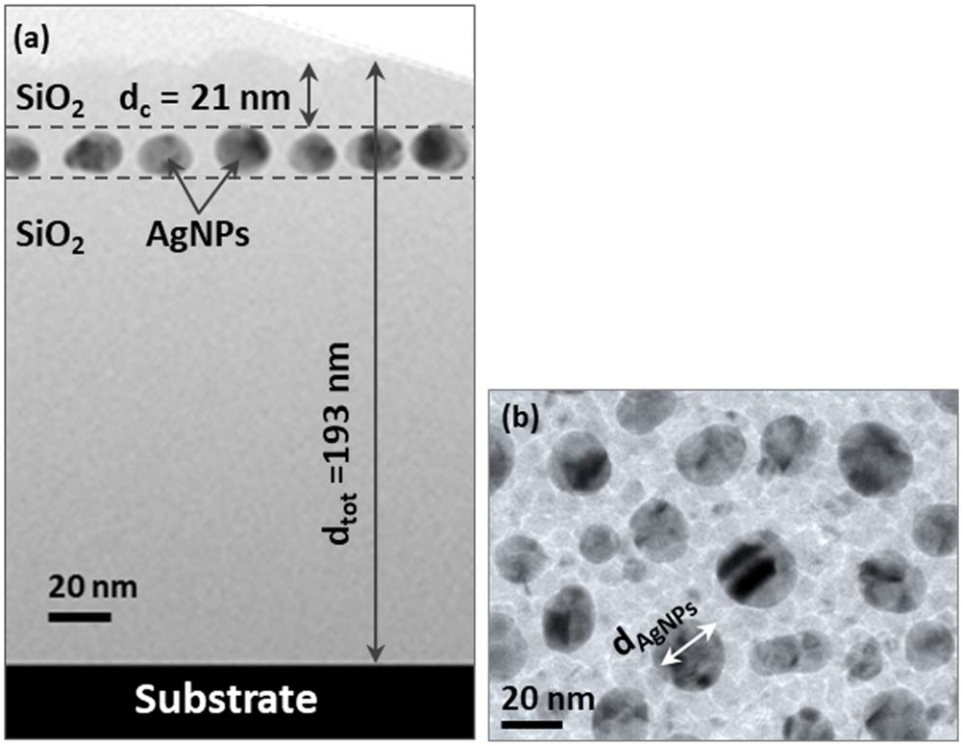

Figure 2. TEM images of the NCs containing a single plane of AgNPs: (a) cross-section view and (b) plane view. The main characteristics of the AgNPs are noted on the images.

transport analyses, the samples were heated at a constant temperature. A temperature range from 25°C to 110°C was selected for the experiments in order to maintain the diffusion of Ag in silica negligible when investigating the electrical charge transport [26–28]. Thus, evaluation of the electrical behaviour of the AgNPs-based nanocomposites without thermally induced structural evolution of the NCs was enabled. The temperature was controlled to 25°C, 50°C, 80°C and 110°C. In order to extract the mean value and the standard deviation of the probed quantities the same charge injection procedure was repeated several times at different location on the sample surface to avoid influence of previous charging.

2.4. Modeling of the electrical behaviour of the AgNPs-based NCs

Investigation of the influence of the embedded single plane of AgNPs on the charge injection at the AFM-tip contact requires knowledge on the electric field distribution in the NCs. To that end, a simple 2D-axisymmetric

Table 1. Parameters of the AgNPs-based NCs. For correspondence, please see figures 1 and 2.

	d_{tot} (nm)	d_{AgNPs} (nm)	d_c (nm)
SiO_2 matrix alone	150.6 ± 1.8	n/a	n/a
NCs with embedded AgNPs-plane	203.0 ± 9.6	19.6 ± 7.8	7.0 ± 1.8
	193.0 ± 8.4	19.6 ± 7.8	21.0 ± 2.0

Finite Element Model (FEM) of the studied structures was developed by using COMSOL Multiphysics®. The model geometry considers the dielectric nanocomposite layer (SiO_2 matrix and the AgNPs-plane), the AFM tip and a surrounding air box whose dimensions are large enough to avoid edge effects. The AFM tip is represented as a 10 μm-height truncated cone (10 μm-height and 14° of aperture angle) ending with a semi-spherical apex (curvature radius $R_c = 25$ nm, the same as the one used in the experiment).

The nanocomposite geometrical parameters: total thickness of the NCs (d_{tot}), size of the AgNPs considered here as spheres of diameter (d_{AgNPs}), distribution of AgNPs in the plane with interparticle distance of 5.0 nm and AgNPs-plane position relative to surface which is actually equal to the thickness of the silica cover layer (d_c) are shown in figures 1 and 2, and are summarized in table 1. They are extracted from measurements of the plasma elaborated NCs. To complete this set of parameters with a limit case, an AgNPs-plane embedded at only 4 nm from the surface of a SiO_2 layer with total thickness $d_{tot} = 200$ nm, is considered in the modeling. The relative dielectric permittivity of the silica layer is taken 3.9 and a floating potential is considered on the AgNPs surface to take into account their metallic nature. The boundary conditions are as follows: V_0 is applied to the AFM tip, the dielectric layer backside is grounded and no charge (zero potential) is applied on the free boundaries of the simulation box. Meshing was refined and optimized close to the contact point of the AFM tip and around the AgNPs.

The Poisson's equation is solved in the air and in the dielectric layer to determine the electric field $\vec{E}$.

$$\overrightarrow{\nabla} \cdot (\varepsilon_0 \varepsilon_r \vec{E}) = \rho, \tag{1}$$

where ε_0 is the vacuum dielectric permittivity, ε_r is the material relative dielectric permittivity and ρ the charge density.

This model is used in two configurations. Configuration 1 computes the spatial distribution of the electric field, during the charge injection step. In this case, the AFM-tip is in contact with the sample surface and the dielectric layer/NCs is considered free of charge (i.e., $\rho = 0$). The axial E_z and the radial E_r components of the electric field as function of the position of the AgNPs-plane in the SiO_2 matrix are extracted from the computed electric field using equation (1). Configuration 2 is applied to investigate the influence of a charge cloud, trapped in the dielectric layer, on the surface potential profile. In this case, the AFM-tip is positioned at 50 nm above the surface and a charge cloud with density distribution ρ is considered in the dielectric layer. This tip-surface distance was fixed by the experimental lift condition applied for the KPFM measurements. Aiming at a description of the injected charge density we have involved in the analysis here a 3D-distribution of the injected charges with a full-Gaussian shape in lateral direction and a half-Gaussian shape in-depth in the dielectric, in accordance with our previous study where homogeneous SiO_2 layers were investigated [35]. Thus, the charge density distribution is given by the following expression:

$$\rho(r, z) = 2Q \frac{1}{\pi\sqrt{2\pi}\sigma_r^2\sigma_z} \exp\left(-\frac{r^2}{2\sigma_r^2} - \frac{z^2}{2\sigma_z^2}\right)$$
$$\text{for } -d_{tot} \leqslant z \leqslant 0 \tag{2}$$

where Q is the injected charge quantity, σ_r is a parameter corresponding to the lateral dimensions of the charge distribution (related to the lateral Full Width at Half-Maximum (FWHM) of the charge density profile, $W_r = 2.35\,\sigma_r$) and σ_z is a parameter describing the in-depth distribution of injected charges (considered here by the in-depth FWHM W_z of the Gaussian curve-shape with $W_z = 2.35\,\sigma_z$).

The electric field $\vec{E}$ is computed using equation (1) and the electrostatic force F_e induced on the tip, by the charge cloud, was deduced from the electric field by using the following equation:

$$F_e = \int\int_{tip} \frac{\varepsilon_0 \varepsilon_r}{2} \|\vec{E}\|^2 \vec{n}.\overrightarrow{dS}, \tag{3}$$

where $\vec{E}$ is the electric field, $\varepsilon_r = 1$ is the air relative dielectric permittivity, $\vec{n}$ the unit vector and $\overrightarrow{dS}$ is an elementary surface. At each point, the electrostatic force F_e is computed as function of the applied bias V_0. Thus, a parabolic curve is obtained and the potential value corresponding to the electrostatic force minimum is

extracted. The so-obtained potential represents the surface potential and is further considered in the study [35, 36].

3. Results and interpretation

3.1. Plasma elaborated AgNPs-based NCs

The morphological analysis of the studied AgNPs-based NCs has been performed by TEM. One of the investigated structures is detailed here. From the TEM cross-section view image in figure 2(a), one can clearly notice that the AgNPs form a planar single layer. The AgNPs-plane is consisted of well aligned NPs, embedded at a nanometric distance ($d_c = 21$ nm) from the surface of the SiO_2 matrix. One can clearly see that the silica matrix envelops the AgNPs and spreads in between them. The total thickness of the structure is $d_{tot} = 193$ nm (table 1). The size of the AgNPs was determined from the plane-view image (figure 2(b)). The AgNPs are of mean size of 19.6 ± 7.8 nm and density of 1.7×10^{11} NPs cm^{-2}, covering an area of 42.6%. The average interparticle distance is of 5.0 nm, which is small enough to facilitate charge transport in-between the AgNPs. A combined analysis from the cross-view and plane-view (figures 2(a) and (b)) brings additional information on the AgNPs morphology aspects. The shape of the AgNPs is rather spherical with a tendency of evolution towards a prolate spheroid, having higher eccentricity of 0.4 for the largest AgNPs. However, the eccentricity level of the AgNPs remains small which allows considering the AgNPs as spherical ones in the model. The AgNPs are randomly distributed in the plane. All the obtained data on the final structures, and on the AgNPs in particular, are in perfect accordance with previously elaborated structures of the type with the same plasma reactor [17, 34].

3.2. Influence of the AgNPs-plane position on charge injection at 25°C

Before going to the analysis of experimental results, we present here the simulation results that emphasize modifications in the electric field distribution in the system induced by the presence of an AgNPs-plane embedded in the SiO_2 matrix at different in-depth positions. The electric field distribution, computed using Configuration 1 of the model (part 2.4) is depicted in figure 3. The actual tip-to-plane geometrical configuration of the system, i.e. AFM-tip in contact with the dielectric layer, imposes a strong inhomogeneity in the electric field distribution. The maximum of the electric field is under the AFM-tip and rapidly decreases in both lateral and in-depth directions. For a homogeneous SiO_2 layer, without AgNPs, the E_z-component is maximum at the contact point and decreases in the volume of the dielectric layer. It is much larger, by three orders of magnitude, than the E_r-component at the contact point. However, in the vicinity of the AFM-tip contact point, because of the interface between the two dielectric media (air and SiO_2 layer), one observes strengthening of the electric field that leads to a maximum of the E_r-component. The E_r-maximum is shifted from the axis in lateral direction (at $r = 5$ nm). Thus, the E_r-component increases strongly close to the injection point and then decreases in lateral direction, although keeping the electric field high even for distances away from the contact point.

Presence of an AgNPs-plane in the silica dielectric layer drastically changes the electric field distribution. Figures 3(a) and (b) show 2D-distributions of the axial E_z and radial E_r components of the electric field in presence of an AgNPs-plane located at only 4 nm from the surface. They reveal that the E_z-component is highest at the contact point and remains very strong in the area between the AgNPs-plane and the SiO_2 surface. Then a field screening effect is observed due to the AgNPs. In the dielectric area below the AgNPs the electric field is strongly decreased, although starting with a value higher than the one corresponding at the same in-depth position in the SiO_2-layer alone (figure 3(c)). The E_r-component, like in the case without AgNPs, is maximum at few nanometers away from the axis. Moreover, due to electrostatic coupling between the AgNPs, the E_r-component of the field is clearly enhanced in the plane in-between the AgNPs. The magnitude of this enhancement of the E_r-component, induced by the AgNPs-coupling, decreases when moving away from the AFM tip.

In presence of an AgNPs-plane in the SiO_2 matrix the modifications of the electric field also depend on the distance, from the dielectric layer surface, at which the AgNPs are embedded. Figure 3(c) compares the profiles of the axial electric field E_z through the dielectric layer for different in-depth positions of the AgNPs-plane. When the AgNPs are embedded away from the dielectric layer surface, at a distance of 21 nm, the axial field distribution near the surface is not significantly changed compared to the SiO_2 matrix alone, although an increase due to the metal nanoparticles is observed at the contact point. The E_z-maximum becomes 3.9×10^9 V m^{-1} in presence of AgNPs compared to 3.1×10^9 V m^{-1} for the bare SiO_2 layer. If the AgNPs-plane is closer to the surface (at 7 nm from the surface), a strong electric field enhancement is observed at the contact point ($E_z = 5.3 \times 10^9$ V m^{-1}) and in the area between the AgNPs-plane and the SiO_2 surface and the maximum of the E_z-component increases. For AgNPs embedded very close to the SiO_2 surface (at only 4 nm) the electric field at the AFM tip contact point is doubled ($E_z = 6.3 \times 10^9$ V m^{-1}). Such strong increase of the electric field at the contact point will favor the dielectric charging in the same way, like if the applied bias is doubled for the bare

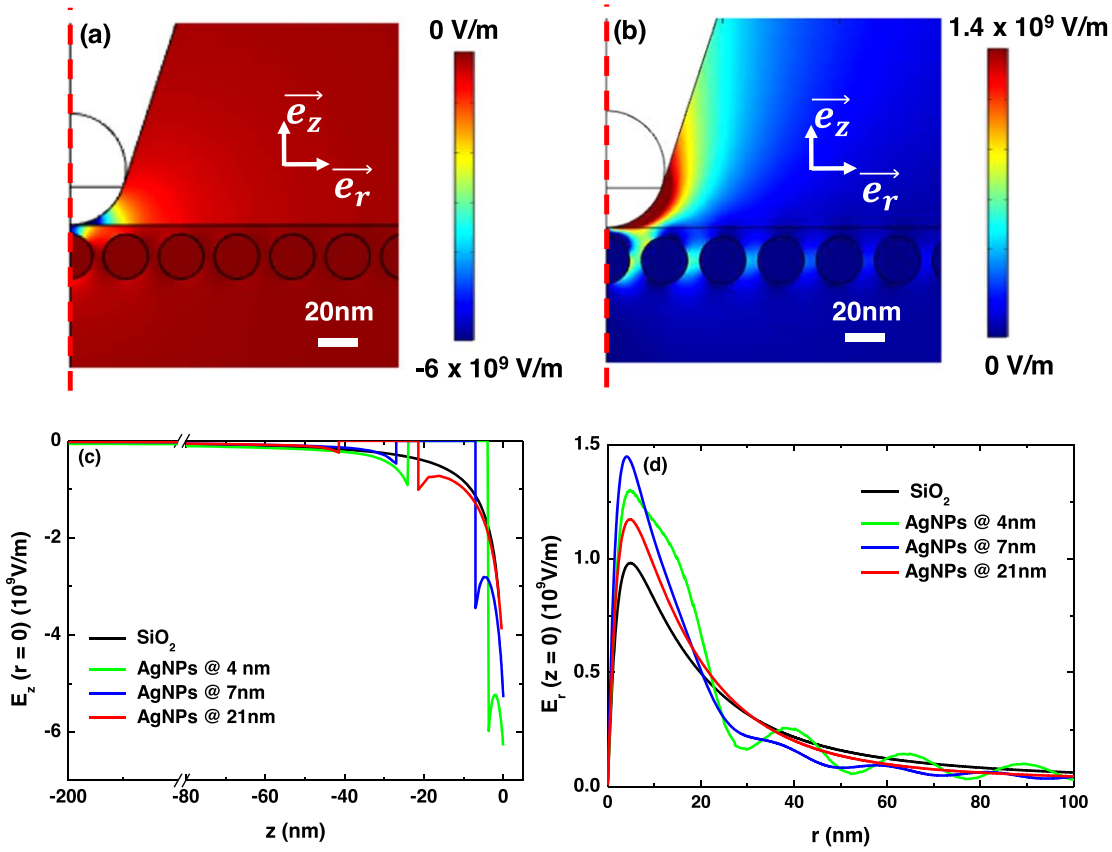

Figure 3. Spatial distribution of computed (a) axial E_z and (b) radial E_r electric field components for $V_0 = 40$ V applied to the AFM tip ($R_c = 25$ nm) during charging of a 200 nm-thick dielectric layer and AgNPs-plane located at 4 nm from the surface. Related (c) E_z distribution along the symmetry axis and (d) E_r distribution at the dielectric/air interface for a 200 nm-thick dielectric layer with AgNPs-plane located at several in-depth positions from the surface.

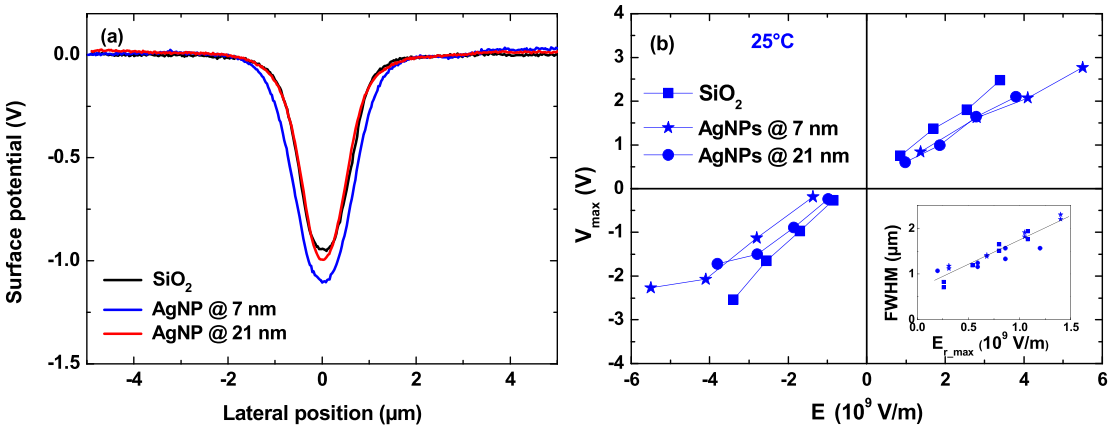

Figure 4. (a) Experimental surface potential profiles after charge injection at −20 V during 1 min, (b) Evolution of the surface potential maximum V_{max} as function of the electric field at the contact point for T = 25°C. Insert: Evolution of the FWHM of the surface potential profiles as function of the maximum of the radial component of the electric field E_{r_max}.

SiO_2 layer. A similar effect of electric field strengthening is observed for the radial electric field E_r (figure 3(d)). When the AgNPs-plane gets closer to the surface (in the range from 21 nm to 7 nm) the E_r maximum increases and its lateral extension becomes smaller under the zone of the AFM tip. When the AgNPs are very close to the surface (i.e., at a distance of only 4 nm), the radial electric field distribution shows different behaviour. The maximum of the field, although higher than the one for bare SiO_2 layer, decreases slightly in comparison with its value for AgNPs-plane positioned at 7 nm from the surface. The reason for such behaviour is the capacitive coupling between the AFM tip and the AgNPs. Although not included in the model, to be confirmed and put forward, one can suggest here a change in the charging mechanism of the AgNPs according to their in-depth

position: direct tunneling for 4 nm, while for 7 nm some of the charges will be trapped in the dielectric and their transport to the AgNPs will be by trap assisted tunneling. A shoulder appears close to the maximum since the coupling of the AFM tip with the second closest AgNP is straighten because of the higher electric field in the air. Oscillations of the E_r-component are observed with minima of the field localized above the AgNPs and maxima in-between them. Indeed, these effects are related to the AgNPs electrostatic coupling that leads to laterally well-defined nodes of the electric field with intensity higher than the one corresponding to the SiO_2 matrix alone. AgNPs, closely situated to the surface, act as internal electrodes towards the AFM tip and concentrate the local electric field. When the distance is larger (more than 21 nm), the capacitive coupling is too weak and the electric field nodes vanish. This capacitive coupling was previously observed while investigating the nanoscale dielectric permittivity of the same AgNPs-based nanocomposites by EFM [30]. Moreover, this coupling effect remains well pronounced even for distances of 100 nm away from the charging point. It means that the conditions for charge spreading in lateral direction are favored by the AgNPs-plane. One should recall here that the interparticle distance is of 5.0 nm, which would allow charge transport by tunneling in-between the AgNPs. In the following, the so-obtained simulation results and the analysis are used for the interpretation of the experimental results.

As mentioned earlier, the measured quantity by KPFM is the surface potential. Figure 4(a) compares the experimentally obtained surface potential profiles, after charge injection at applied bias of −20 V during 1 min for the AgNPs-based NCs and the bare SiO_2 layer. As shown in it, regardless the sample nature, a classical Gaussian shape is obtained for all surface potential profiles. From general considerations, one can state that the area of the surface potential profiles reflects the quantity of injected charges when the charges remain trapped in the dielectric, close to the injection point [17]. However, the latter stands for homogeneous amorphous dielectric layers. When dealing with NCs, as the case here, this assumption shall be revised. Second consideration is that the maximum of the surface potential V_{max} and the FWHM of the obtained potential profiles are related to the lateral spreading of the injected charges in the dielectric. In this study, the V_{max} and the FWHM are extracted from the experimental surface potential profiles (figure 4(b)). As emphasized by results reported in the literature for bare SiO_2 thin layers [37], the charge generation is controlled by the electric field at the contact point, mainly by the E_z-component. But the presence of an AgNPs-plane in the SiO_2 matrix, in proximity to its surface, enhances the electric field at the contact point, according to the modeling results obtained here (figure 3). This electric field enhancement is well revealed by the experimental surface potential profiles, shown in figure 4(a). When the AgNPs are located close to the SiO_2 surface (at 7 nm) the surface potential profile has a larger area and a higher maximum V_{max}. Considering also the coupling in-between the AgNPs the FWHM of the surface potential profile is larger in this case. When the AgNPs are deeply embedded in the SiO_2 matrix (at 21 nm in-depth) the recorded surface potential profile repeats almost identically the one for the bare SiO_2 layer. The maximum V_{max} is slightly higher due to a slightly increased electric field at the contact point, mainly the E_z-component (figure 3(c)). Such field-dependent behaviour invalidates any analysis of the charge injection mechanisms in nanocomposite dielectrics based only on comparison of experimentally obtained surface potential profiles as function of the applied bias on the AFM-tip at the charging point, as typically performed for homogeneous dielectric layers [30, 37–39]. The heterogeneity of the structure of the studied AgNPs-based NCs induces a coupling between the AgNPs and the AFM tip that results in an enhancement of the electric field, so the analysis of charge injection mechanisms requires knowledge of the electric field at the contact point in this case. Accordingly, the experimental results are discussed hereafter by considering an effective applied electric field as computed from the model (figure 3).

Figure 4(b) compares the evolution of the experimental surface potential maximum V_{max} as function of the simulated electric field at the contact point for the bare SiO_2 layer and the AgNPs-based NCs. At 25°C, the surface potential maximum V_{max} increases with the electric field at the contact point for all structures. For negative injected charges, the same behavior is observed for the bare SiO_2 and for the nanocomposite with AgNPs located at 21 nm from the surface. However, when looking for a fixed electric field, the presence of AgNPs close to surface (i.e., AgNPs-plane located at 7 nm) leads to a decrease of V_{max} compared to bare SiO_2 layer. For positive injected charges, a slightly different behavior is observed. Indeed, the same evolution is observed for both NCs, whose surface potential maxima remain lower than the one for bare SiO_2 layer at a fixed electric field. No clear dependence can be found for the FWHM in presence or not of AgNPs-plane. Since the radial component of the electric field drives the charge spreading, the FWHM increases with the radial electric field maximum E_{r_max}, but remains insensitive to AgNPs-plane position in the SiO_2 layer (insert in figure 4(b)).

Again, due to the electric field enhancement in presence of an AgNPs-plane close to the dielectric layer surface and the dependence of the level of enhancement on the in-depth position of the AgNPs-plane, the charging kinetics requires analysis with regard to the same electric field, and not to the same applied bias. Therefore, one observes inversion of the trends, i.e., for a fixed electric field, the presence of an AgNPs-plane close to the surface (i.e., AgNPs-plane located at 7 nm) leads to a lower V_{max} than the one corresponding to the bare SiO_2 layer. This is preserved regardless the charge polarity. Two hypotheses can be risen, in order to explain

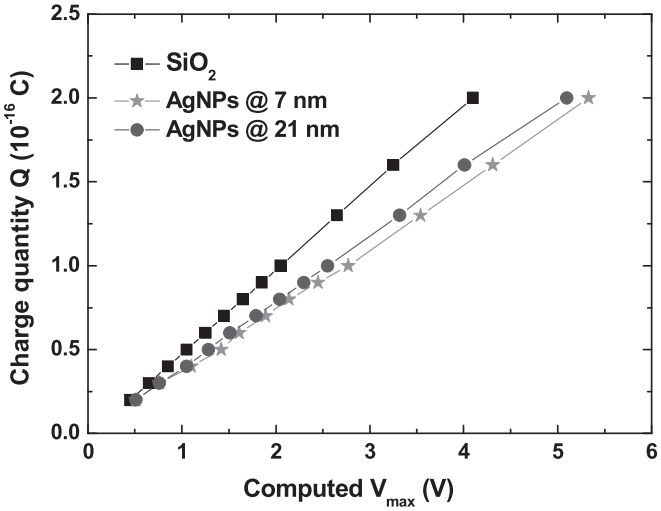

Figure 5. Evolution of the charge quantity Q ($W_z = 10$ nm and $W_r = 1\ \mu$m) as function of the computed surface potential maximum V_{max}.

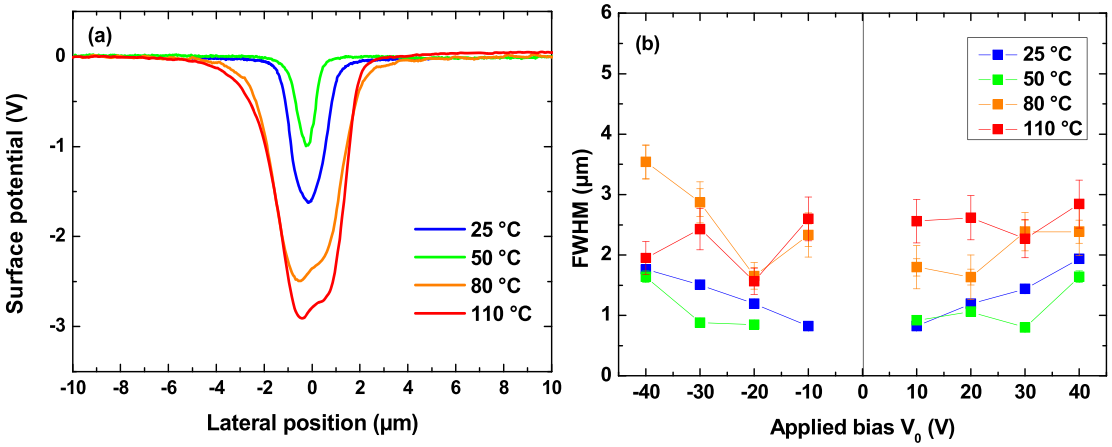

Figure 6. (a) Comparison of surface potential profiles after a charge injection at −30 V during 1 min for various temperatures in bare SiO_2 sample, (b) Temperature influence on the evolution of the FWHM as function of the applied bias V_0. At low temperatures (25°C–50°C), the error bars are small enough not to exceed the size of the symbols.

Table 2. Experimental surface potential maximum V_{max} and the related computed charge quantity Q for both positive and negative electric field E at the contact point ($W_z = 10$ nm and $W_r = 1\ \mu$m).

	$E = -2.5 \times 10^9$ V m^{-1}		$E = 2.5 \times 10^9$ V m^{-1}	
	V_{max} (V)	Q (10^{-16} C)	V_{max} (V)	Q (10^{-16} C)
SiO_2	−1.8	−0.9	1.8	0.9
AgNPs @ 7 nm	−1.0	−0.4	1.5	0.55
AgNPs @ 21 nm	−1.4	−0.59	1.5	0.62

this surface potential decrease when the AgNPs-plane gets closer to the dielectric surface: (i) lower injected charge density compared to the one in the bare SiO_2 layer and/or (ii) electrostatic screening effect induced by the AgNPs-plane.

Aiming at an identification of the relative contribution of the injected charge density and the screening effect exerted by the AgNPs, the surface potential is computed in presence of a charge cloud. To that end, Configuration 2 of the developed model was employed to consider the 3D in-depth distribution of the injected

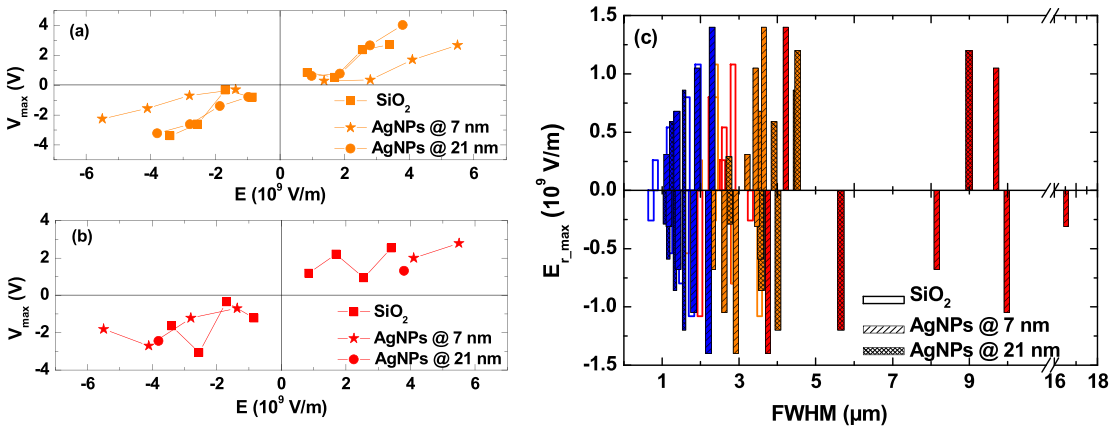

Figure 7. Evolution of the surface potential maximum V_{max} as function of electric field at the contact point for (a) T = 80°C and (b) T = 110°C. In (c) FHWM at T = 25°C (blue), T = 80°C (orange) and T = 110°C (red) attained for the corresponding E_{r_max}.

charge cloud $\rho(r, z)$ in the dielectric layer (equation (2)). Figure 5 represents the evolution of the injected charge quantity Q for $W_z = 10$ nm and $W_r = 1$ μm as function of the computed surface potential maximum. By applying these values describing the Gaussian distribution of injected charges to the SiO_2 and to the two AgNPs-based NCs one obtains FWHM for the potential profile of around 2 μm for both types of samples which is comparable to the experimentally obtained FWHM, reported in the insert of figure 4(b). As expected, the computed surface potential maximum increases when the injected charge quantity Q is larger. For a fixed Q, the computed V_{max} increases with decreasing of the distance between the AgNPs-plane and the surface. Considering the hypothesis of identical in-depth spreading of the charge cloud for all samples (i.e., $W_z = 10$ nm), the charge quantities Q corresponding to the experimental surface potential maximum for both positive and negative electric field at the contact point are determined and summarized in table 2. According to these results, it is worth noticing that a smaller charge quantity is injected when the AgNPs-plane gets closer to the dielectric surface. Consequently, at 25°C the presence of the AgNPs limits the amount of stored charge in the dielectric layer, and this limitation is reinforced when the distance between the AgNPs-plane and the dielectric surface decreases. This finding also explains the lower experimentally obtained V_{max} for a fixed electric field at the contact point for AgNPs closely located to the dielectric surface (figure 4(b)).

3.3. Charge injection in AgNPs-based NCs at higher temperature (50°C–110°C)

To identify the impact of the AgNPs-plane embedded in SiO_2 on charge injection when the temperature is increased, our analysis starts with the bare SiO_2 layer. Figure 6(a) compares the experimentally obtained surface potential profiles, at different temperatures, after charge injection at applied bias of −30 V during 1 min in the bare SiO_2 sample. Regardless the temperature value, a classical Gaussian shape is obtained for all surface potential profiles. Figure 6(a) emphasizes that the peak maximum and the profile width increase with the temperature. It means that a larger quantity of charges is injected in the bare SiO_2 layer for higher temperatures. To go further in the interpretation, the FWHM of the obtained potential profiles is depicted as function of the applied bias V_0 (figure 6(b)). The standard deviation on FWHM is strongly impacted by the temperature and is equal to 6% at 25°C, to 8% at 50°C, to 14% at 80°C and to 18% at 110°C. This increase of the standard deviation can be related to instabilities of the AFM tip induced by the heating. The FWHM increases linearly with the applied bias at low temperatures (25°C–50°C). This increasing is similar for positive and negative bias, which implies that the same injection dynamic drives both types of charges, electrons and holes. Similar behaviour was already observed, at 25°C, for charge injection, using Pt-coated AFM tip in a 40 nm-thick SiO_xN_y layers, containing a very small amount of N (only 4 at.%) and exhibiting structural and optical properties very close to a SiO_2 layer. These dielectric layers were processed by a pulsed PECVD. More details on this study can be found elsewhere [35]. At higher temperatures (80°C–110°C) and for a given bias, the FWHM of the obtained surface potential profiles is larger than the one at 25°C. However, according to the high standard deviation, the FWHM seems without clear dependence on the applied bias V_0 for higher temperatures. The surface potential profile amplitude and width result in a steady state between two adversely contributing mechanisms which are charge injection and transport. In the temperature (25°C–110°C) and electric field (up to few 10^9 V m^{-1}) ranges, the charge injection by an AFM tip is sustained by the mutual action of thermionic and field electron emission mechanisms [37]. In this case, the charge injection is described in the frame of the Fowler-Nordheim theory. While the field dependence occurs in the shape of the potential barrier at the metal/dielectric interface, the temperature dependence arises in the assumed Fermi distribution function for a free electron gas in the metal.

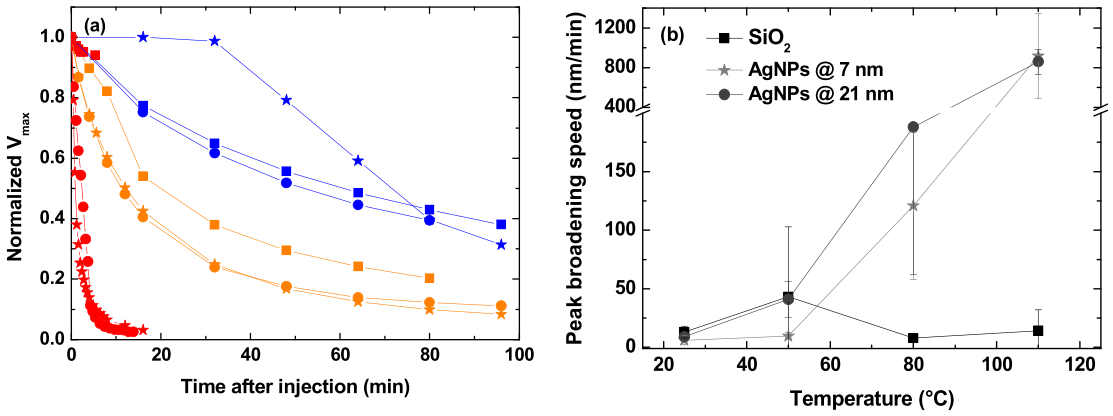

Figure 8. (a) Evolution of the normalized potential maximum V_{mn} as function of time after injection (1 min at −40 V) at T = 25°C (blue), T = 80°C (orange) and T = 110°C (red). Bare SiO_2, AgNPs-plane at 7 nm and 21 nm are represented by squares, stars and circles, respectively. (b) Evolution of the peak broadening speed as function of temperature.

Although the maximum of the distribution function holds to the Fermi level, when increasing the temperature electrons at energies above the Fermi level become available, and the charge injection in the dielectric is increased. Moreover, the FWHM is increased only twice when passing from 25°C to 110°C implying that the lateral charge transport remains limited. This is further confirmed by low peak broadening speed, reported later on. Obviously here, the maximum of the surface potential increases with the temperature, meaning that the injected charge is substantially increased while the charge transport is limited.

The picture changes in presence of an AgNPs-plane embedded closely to the dielectric surface. Figure 7 compares the evolution of the surface potential maximum V_{max} as function of the electric field at the contact point and the corresponding FWHM as function of the radial electric field maximum for various temperatures. The standard deviation of the surface potential maximum is strongly impacted by the temperature increase, corresponding to 16% and 20% at 80°C and 110°C, respectively. Regardless of the temperature variation, the surface potential maximum increases with the electric field at the contact point. Increasing the temperature up to 80 °C does not imply changes in the behaviour of the injected charges. It remains the same as observed at 25°C (figure 4(b) versus figure 7(a)). Indeed, for a given electric field, due to the presence of AgNPs-plane close to surface (i.e., AgNPs-plane located at 7 nm) the V_{max} decreases, if compared to the bare SiO_2 layer or to the AgNPs-plane embedded at 21 nm away from the surface. This behavior is observed for both positive and negative charges. It can be related to a lower amount of injected charges in the nanocomposite than in the bare SiO_2 like for low temperatures. Moreover, the FWHM is slightly larger for the AgNPs-based NCs compared to the bare SiO_2 layer (figure 7(c)). It means that at 80 °C the presence of AgNPs limits slightly the amount of stored charges in the dielectric layer only when the AgNPs-plane is closely situated to surface (i.e., at 7 nm). At 110°C, the evolution of the surface potential maximum V_{max} with the electric field at the contact point is similar for all structures. Besides, at this high temperature, the FWHM is substantially higher for the AgNPs-based NCs compared to the SiO_2 (figure 7(c)). This implies that due to the AgNPs a higher charge quantity is injected at 110°C in the NCs than in the bare SiO_2.

3.4. Charge dynamic in the AgNPs-based NCs

The charge dynamic after injection was studied by following two parameters: the normalized maximum potential V_{mn} with respect to its initial values (figure 8(a)) and the peak broadening speed which corresponds to the slope of the characteristic FWHM as function of time. This slope was computed for each injection bias V_0. The mean value of the peak broadening speed alongside with its standard deviation is depicted on figure 8(b). First of all, one shall say that the same behavior is observed for both positive and negative charges. For simplicity only the negative charge dynamic is presented on the figure. At 25°C, the normalized surface potential maximum decreases with the same dynamic for the bare SiO_2 and the nanocomposite with AgNPs-plane located at 21 nm from the surface. Concerning the nanocomposite with AgNPs-plane embedded at 7 nm from the surface, one observes that the V_{mn} remains almost constant during 38 min after the end of charge injection. It means that the AgNPs retain the trapped charges for a long time, i.e. the trapped charge stability is strong. At 25°C, the peak broadening speed is equal to 13 $\pm$ 5 nm min^{-1} for the bare SiO_2, and to 6 $\pm$ 3 nm min^{-1}, and 9 $\pm$ 3 nm min^{-1} for the nanocomposites with AgNPs-plane located at 7 nm and 21 nm, respectively (figure 8(b)). This implies that the lateral charge spreading is lower for the AgNPs-based NCs compared to the

bare SiO_2 layer. The reported here values are in the same order of magnitude as the ones obtained by Lwin [31] for AuNPs and PtNPs embedded in SiO_2 matrix. Indeed, a peak broadening speed of 5.4 nm min^{-1} and 1.5 nm min^{-1} was reported for Au- and Pt- nanoparticles, respectively. The same behavior is observed at 50°C. For temperatures higher than 80°C the decrease of V_{mn} is faster and faster, for both the bare SiO_2 layer and the NCs. The peak broadening speed appears rather independent from the temperature increase for the bare SiO_2 layer whereas it strongly increases for the AgNPs-based NCs, especially for temperatures higher than 50°C.

4. Conclusion

In this study we addressed the impact of a single plane of AgNPs embedded in a SiO_2 layer close to its surface on the electric field distribution, the charge injection and the charge dynamic processes for different AgNPs-based NCs and various temperatures in the range 25°C–110°C. The AgNPs-plane is embedded in the SiO_2 matrix at different depths from the surface. The AgNPs are randomly distributed in the plane with interparticle distances allowing charge transport in-between the NPs. The NCs are elaborated by plasma deposition and are with well-controlled characteristics. These stratified structures are actually model structures that allow reducing the 3D problem of nanoparticles dispersed in the dielectric matrix to a 2D-one for which the AgNPs are aligned in a plane and located at well-controlled distance from the surface. Electrostatic modelling by FEM of these heterogeneous structures and measurements by KPFM of the surface potential after charge injection are combined to reveal the impact of the AgNPs on the electric field distribution and consequently, on the processes of charge injection. It is found that a strong coupling between the AFM tip and the AgNPs exists when the AgNPs-plane is located close to the AFM tip (i.e., less than 7 nm) and leads to a strong enhancement of the electric field in that region of the dielectric. The FEM modeling allows quantification of the electric field enhancement close to the contact point of the AFM tip. Depending on the applied bias, this enhancement might be more than a factor of two. Moreover, this phenomenon is favored when the AgNPs-plane gets closer to the dielectric surface. As far as the charge injection dynamic is concerned, the presence of an AgNPs-plane close to the surface (i.e., distance of 7 nm), limits the amount of injected charges for temperatures up to 80°C, when compared to the SiO_2 alone. At 110°C the amount of injected charge is increased in the AgNPs-based NCs, and all structures present similar behavior, even though the lateral spreading is limited for SiO_2. The charge stability after charge injection at 25°C is improved for the AgNPs-based NCs compared to the bare SiO_2 layer because of the strong capability of AgNPs to store electrical charges, revealed by the very low speed for the charge lateral spreading. At high temperatures, the peak broadening speed increases for the NCs which implies that the lateral charge transport is favored due to the electric field coupling between the closely situated AgNPs in the plane. The introduction of AgNPs therefore induces an enhanced sensitivity of the charge storage to temperature variations compared to SiO_2, thereby opening ways to temperature-sensible device applications.

Acknowledgments

This work was supported by the program IDEX Actions Thématiques Stratégiques—ATS 2015 of the Université de Toulouse under project SEPHIR (2016-066-CIF-D-DRVD).

Data availability statement

All data that support the findings of this study are included within the article (and any supplementary files).

Competing interests

The authors declare that they have no competing interests.

ORCID iDs

C Villeneuve-Faure https://orcid.org/0000-0002-7959-2912
K Makasheva https://orcid.org/0000-0001-6113-3593
L Boudou https://orcid.org/0000-0001-5339-2042
G Teyssedre https://orcid.org/0000-0001-6684-0262

References

[1] Ahopelto J *et al* 2019 Nano electronics roadmap for Europe: from nanodevices and innovative materials to system integration *Solid-State Electron.* **155** 7

[2] Ahmad I, Siquidi W A, Ahmad T and Siddiqui V U 2019 Synthesis and characterization of molecularly imprinted ferrite (SiO_2@Fe_2O_3) nanomaterials for the removal of nickel (Ni^{2+} ions) from aqueous solution *Journal of Materials Research and Technology* **8** 1400

[3] Vaidya S, Ahmad T, Agarwal S and Ganguli A K 2007 Nanocrystalline oxalate/carbonate precursors of Ce and Zr and their decompositions to CeO_2 and ZrO_2 nanoparticles. *J. Am. Ceram. Soc.* **90** 863

[4] Gupta S *et al* 2019 Low Power, CMOS-MoS_2 memtransistor based neuromorphic hybrid architecture for wake-up systems *Sci. Rep.* **9** 15604

[5] Jenkins M *et al* 2019 Review—beyond the highs and lows: a perspective on the future of dielectrics research for nanoelectronic devices *ECS J. Solid State Sci. Technol.* **8** N159

[6] Liu J and Koide Y 2018 Overview of high-k oxides on hydrogenated diamond for metal-oxide-semiconductor capacitors and field-effect transistors *Sensors* **18** 1813

[7] Kiesow A, Morris J E, Radehaus C and Heilmann A 2003 Switching behavior of plasma polymer films containing silver nanoparticles *J. Appl. Phys.* **94** 6988

[8] Gong M L and Wan P 2020 Polymer nanocomposite meshes for flexible electronic devices *Prog. Polym. Sci.* **107** 101279

[9] Zang X, Zhou Q, Chang J, Liu Y and Lin L 2015 Graphene and carbon nanotube (CNT) in MEMS/NEMS applications *Microelectron. Eng.* **132** 192

[10] Wang L, Huang X, Yingke Zhu Y and Jiang P 2018 Enhancing electrical energy storage capability of dielectric polymer nanocomposites via the room temperature coulomb blockade effect of ultra-small platinum nanoparticles *Phys. Chem. Chem. Phys.* **20** 5001

[11] Kapetanakis E *et al* 2000 Charge storage and interface states effects in Si-nanocrystal memory obtained using low-energy implantation and annealing *Appl. Phys. Lett.* **77** 3450

[12] Busseret C, Souifi A, Baron T, Monfray S, Buffet N, Gautier E and Semeria M N 2002 Electronic properties of silicon nanocrystallites obtained by SiO_x ($x < 2$) annealing *Mater. Sci. Eng., C* **19** 237

[13] Yater J 2020 Implementation of Si nanocrystals in non-volatile memory devices *Physica status solidis* **210** 1505

[14] Benguedouara Y, Keghouchea N and Belloni J 2012 Structural and magnetic properties of Ni–Pt nanoalloys supported on silica *J. Mater. Sci. Eng. B* **177** 27

[15] Ye Y H, Jiang Y W, Tsai M W, Chang Y T, Chen C Y, Tzuang D C, Wu Y T and Lee S C 2008 Localized surface plasmon polaritons in $Ag/SiO_2/Ag$ plasmonic thermal emitter *Appl. Phys. Lett.* **93** 033113

[16] Cacciato G, Bayle M, Pugliara A, Bonafos C, Zimbone M, Privitera V, Grimaldia M G and Carles R 2015 Enhancing carrier generation in TiO_2 by a synergistic effect between plasmon resonance in Ag nanoparticles and optical interference *Nanoscale* **7** 13468

[17] Makasheva K, Villeneuve-Faure C, Bonafos C, Laurent C, Pugliara A, Despax B, Boudou L and Teyssedre G 2016 Dielectric engineering of nanostructured layers to control the transport of injected charges in thin dielectrics *IEEE Trans. Nanotechnol.* **15** 839

[18] Racles C, Nistor A and Cazacu M 2013 A silica-silver nanocomposite obtained by sol-gel method in the presence of silver nanoparticles *Cent. Eur. J. Chem.* **11** 1689

[19] Laurent C, Kay E and Souag N 1988 Dielectric breakdown of polymer films containing metal clusters *J. Appl. Phys.* **64** 336

[20] Canet P, Laurent C, Akinnifesi J and Despax B 1992 Dielectric properties of gold containing plasma polymerized thin films *J. Appl. Phys.* **72** 2423

[21] Wei H and Eilers H 2008 Electrical conductivity of thin-film composites containing silver nanoparticles embedded in a dielectric fluoropolymer matrix *Thin Solid Films* **517** 575

[22] Milliere L, Makasheva K, Laurent C, Despax B, Boudou L and Teyssedre G 2015 Silver nanoparticles as a key feature of a plasma polymer composite layer in mitigation of charge injection into polyethylene under dc stress *J. Phys. D: Appl. Phys.* **49** 15304

[23] Luo S, Yu S, Sun R and Wong C-P 2014 Nano Ag-deposited $BaTiO_3$ hybrid particles as fillers for polymeric dielectric composites: toward high dielectric constant and suppressed loss *ACS Appl. Mater. Interfaces* **6** 176

[24] Banerjee S and Chakravorty D 1999 Electrical resistivity of silver-silica nanocomposites *J. Appl. Phys.* **85** 3623

[25] Fan F, Liu F, Yang G, Li H, Zhang G, Jiang S and Wang Q 2018 Dielectric materials for high-temperature capacitors *IET Nanodielectr.* **1** 32

[26] McBrayer J D, Swanson R M and Sigmon T W 1986 Diffusion of metals in silicon dioxide *J. Electrochem. Soc.* **133** 1242

[27] Coffa S, Poate J M, Jacobson D C, Frank W and Gustin W 1992 Determination of diffusion mechanisms in amorphous silicon *Phys. Rev. B* **45** 8355

[28] Carrada M, Salem A H, Pecassou B, Carles R and Ben Assayag G 2017 Hybrid systems with Ag nanocrystals and Si nanostructures synthesized by ultra-low-energy ion beam synthesis *J. Appl. Phys.* **122** 103101

[29] Riedel C, Arinero R, Tordjeman P, Ramonda M, Lévêque G, Schwartz G A, de Oteyza D G, Alegria A and Colmenero J 2009 Determination of the nanoscale dielectric constant by means of a double pass method using electrostatic force microscopy *J. Appl. Phys.* **106** 024315

[30] Villeneuve-Faure C, Makasheva K, Djaou C, Boudou L and Teyssedre G 2018 Characterization of the electrical behaviour of thin dielectric films at nanoscale using methods derived from atomic force microscopy: application to plasma deposited AgNPs-based nanocomposites *Proc. of the IEEE 13th Nanotechnology Materials and Devices Conf. (NMDC)* (https://doi.org/10.1109/NMDC.2018.8605887)

[31] Lwin Z, Pey K L, Liu C, Liu Q, Zhang Q, Chen Y, Singh P K N and Mahapatra S 2011 Localized charge trapping and lateral charge diffusion in metal nanocrystal-embedded High-κ/SiO_2 gate stack *Appl. Phys. Lett.* **99** 222102

[32] Schaadt D M, Yua E T, Sankar S and Berkowitz A E 1999 Charge storage in Co nanoclusters embedded in SiO2 by scanning force microscopy *Appl. Phys. Lett.* **74** 472

[33] Tzeng S D and Gwo S 2006 Charge trapping properties at silicon nitride/silicon oxide interface studied by variable-temperature electrostatic force microscopy *J. Appl. Phys.* **100** 023711

[34] Pugliara A, Bonafos C, Carles R, Despax B and Makasheva K 2015 Controlled elaboration of large-area plasmonic substrates by plasma process *Mater. Res. Express* **2** 065005

[35] Mortreuil F, Boudou L, Makasheva K, Teyssedre G and Villeneuve-Faure C 2021 Influence of dielectric layer thickness on charge injection, accumulation and transport phenomena in thin silicon oxynitride layers: a nanoscale study *Nanotechnology* **32** 065706

[36] Charrier D S H, Kemerink M, Smalbrugge B E, Vries T and Janssen R A J 2008 Real versus measured surface potentials in scanning Kelvin Probe Microscopy *ACS Nano* **2** 622

[37] Villeneuve-Faure C, Makasheva K, Boudou L and Teyssedre G 2016 Charge injection in thin dielectric layers by atomic force microscopy: influence of geometry and material work function of the AFM tip on the injection process *Nanotechnology* **27** 245702
[38] Ressier L and Le Nader V 2008 Electrostatic nanopatterning of PMMA by AFM charge writing for directed nano-assembly *Nanotechnology* **19** 135301
[39] Vianello E, Nowak E, Mariolle D, Chevalier N, Perniola L, Molas G, Colonna J P, Driussi F and Selmi L 2010 Direct probing of trapped charge dynamics in SiN by Kelvin Force Microscopy *2010 Int. Conf. on Microelectronic Test Structures (ICMTS)* pp 94–7